Research
A SCIENCE PARTNER JOURNAL

RESEARCH ARTICLE

Particle Size-Controlled Oxygen Reduction and Evolution Reaction Nanocatalysts Regulate Ru(bpy)$_3^{2+}$'s Dual-potential Electrochemiluminescence for Sandwich Immunoassay

Shijun Wang[1†], Shu Zhu[1†], Ziqi Kang[1†], Xiangxiu Wang[2], Zixin Deng[1], Kun Hu[1], Jianjun Hu[5], Xiancheng Liu[2], Guixue Wang[2,3*], Guangchao Zang[1,3,4*], and Yuchan Zhang[1,3*]

[1]Institute of Life Science and Laboratory of Tissue and Cell Biology, Lab Teaching & Management Center, Chongqing Medical University, Chongqing 400016, China. [2]Key Laboratory for Biorheological Science and Technology of Ministry of Education, State and Local Joint Engineering Laboratory for Vascular Implants, Bioengineering College of Chongqing University, Chongqing 400030, China. [3]Jinfeng Laboratory, Chongqing 401329, China. [4]Department of Pathophysiology, Chongqing Medical University, Chongqing 400016, China. [5]Department of Pathology, Guizhou Provincial People's Hospital, Guiyang, Guizhou 550002, China.

*Address correspondence to: wanggx@cqu.edu.cn (G.W.); zangguangchao@cqmu.edu.cn (G.Z.); zhangyc@cqmu.edu.cn (Y.Z.)
†These authors contributed equally to this work.

Citation: Wang S, Zhu S, Kang Z, Wang X, Deng Z, Hu K, Hu J, Liu X, Wang G, Zang G, Zhang Y. Particle Size-Controlled Oxygen Reduction and Evolution Reaction Nanocatalysts Regulate Ru(bpy)$_3^{2+}$'s Dual-potential Electrochemiluminescence for Sandwich Immunoassay. *Research* 2023;6:Article 0117. https://doi.org/10.34133/research.0117

Submitted 16 October 2022
Accepted 19 March 2023
Published 14 April 2023

Shijun Wang et al. Exclusive Licensee Science and Technology Review Publishing House. No claim to original U.S. Government Works. Distributed under a Creative Commons Attribution License (CC BY 4.0).

Multiple signal strategies remarkably improve the accuracy and efficiency of electrochemiluminescence (ECL) immunoassays, but the lack of potential-resolved luminophore pairs and chemical cross talk hinders their development. In this study, we synthesized a series of gold nanoparticles (AuNPs)/reduced graphene oxide (Au/rGO) composites as adjustable oxygen reduction reaction and oxygen evolution reaction catalysts to promote and modulate tris(2,2′-bipyridine) ruthenium(II) (Ru(bpy)$_3^{2+}$)'s multisignal luminescence. With the increase in the diameter of AuNPs (3 to 30 nm), their ability to promote Ru(bpy)$_3^{2+}$'s anodic ECL was first impaired and then strengthened, and cathodic ECL was first enhanced and then weakened. Au/rGOs with medium-small and medium-large AuNP diameters remarkably increased Ru(bpy)$_3^{2+}$'s cathodic and anodic luminescence, respectively. Notably, the stimulation effects of Au/rGOs were superior to those of most existing Ru(bpy)$_3^{2+}$ co-reactants. Moreover, we proposed a novel ratiometric immunosensor construction strategy using Ru(bpy)$_3^{2+}$'s luminescence promoter rather than luminophores as tags of antibodies to achieve signal resolution. This method avoids signal cross talk between luminophores and their respective co-reactants, which achieved a good linear range of 10^{-7} to 10^{-1} ng/ml and a limit of detection of 0.33 fg/ml for detecting carcinoembryonic antigen. This study addresses the previous scarcity of the macromolecular co-reactants of Ru(bpy)$_3^{2+}$, broadening its application in biomaterial detection. Furthermore, the systematic clarification of the detailed mechanisms for converting the potential-resolved luminescence of Ru(bpy)$_3^{2+}$ could facilitate an in-depth understanding of the ECL process and should inspire new designs of Ru(bpy)$_3^{2+}$ luminescence enhancers or applications of Au/rGOs to other luminophores. This work removes some impediments to the development of multisignal ECL biodetection systems and provides vitality into their widespread applications.

Introduction

Electrochemiluminescence immunoassay (ECLIA) is an advanced technology for detecting ultratrace amounts of active substances. It combines high-sensitivity chemiluminescence determination, highly controllable electrochemical analysis, and highly specific immune reactions [1,2]. However, most ECL analysis systems are based on a single signal mode (either "signal-on" or "signal-off" mode), which deteriorates the stability, accuracy, and efficiency of the signal output, as well as the integration and miniaturization of biosensors [3]. Multisignal output strategies achieve better detection efficiency and accuracy of the sensor when incorporated

into the application of signal self-calibration or the simultaneous detection of multiple markers [4]. Multiple-signal ECL outputs rely on the introduction of resolvable signal output probes, with the potential-resolved strategy being the most widely used because of its reduced instrument requirements, accelerated test times, and enhanced sample throughput [5]. However, potential-resolved-based multisignal ECL systems are often plagued by the limited choices of luminophore pairs and mutual cross talk in or between co-reactants and luminophores [6,7]. Therefore, the development and simplification of a potentially resolvable ECL system is urgently needed for the further development of multisignal output platforms.

Previous studies showed that many single luminophores can produce dual ECL signals under different potentials in the presence of corresponding co-reactants, which can be utilized to build a dual-signal output ECL system [8]. Relevant research on single-luminophore-based potential-resolved systems can be divided into 2 categories, as reported in our previous study [9]. The first type relies on special chemical reactions between the metallic analytes and luminous systems. Cao et al. [10] used tris(2,2′-bipyridine) ruthenium(II) ($Ru(bpy)_3^{2+}$) as the only emitter with a cathodic co-reactant, Au-g-C_3N_4NSs on electrode, to achieve rapid ratiometric detection of Hg^{2+} by in situ generation of gold (Au) amalgam to produce anodic co-reactant g-C_3N_4NSs. The second type of system relies only on a single emitter and a single co-reactant, attaining the simplest ratiometric ECL system, where the ratio of the dual signal with a single-directional change at separate potentials was used as the output signal [11]. However, single-emitter systems with separate signal conversion designed for biomaterials (such as proteins, aptamers, and cells) are rarely reported owing to the high demand for self-resolved emission systems without the assistance of chemical reactions with analytes.

Hence, we innovatively introduced a series of similar co-reactants to realize the conversion of the anode and cathode signal outputs using $Ru(bpy)_3^{2+}$ as a single luminophore. Recent reports have revealed that the cathodic process of $Ru(bpy)_3^{2+}$ is related to the oxygen reduction reaction (ORR), and the generation of reactive oxygen species (ROS) can remarkably enhance luminescence [10]. Evidence has shown that the anodic process can be quenched by O_2 while being enhanced by •OH, which is the final product and intermediate product of the oxygen evolution reaction (OER) process, the reverse reactions of the ORR [12]. Therefore, Au nanoparticles (AuNPs), acting as an ORR and OER catalyst, where their catalytic performance can be adjusted by their particle size [13–15], will act as an ideal reagent to regulate the anodic and cathodic luminescence of $Ru(bpy)_3^{2+}$ by producing different ROS (Fig. 1). However, using AuNPs alone can lead to blockage of the electron transfer by capping agents and restricted durability owing to their high surface energy [16–19]. Hence, in situ growth of Au on specific supports can be more desirable. As a robust 2-dimensional material combined with high surface-to-volume ratio, high conductivity, and good stability, reduced graphene oxide (rGO) is an ideal platform for growing or anchoring functional nanomaterials [20–22].

In this study, we proposed a new, facile, and low-cost approach to synthesize a series of Au/rGOs with different AuNP particle sizes and to measure their ORR and OER activities and their effects on the luminescence of $Ru(bpy)_3^{2+}$. We then systematically clarified the detailed mechanisms of the conversion of the anodic or cathodic luminescence of $Ru(bpy)_3^{2+}$ by controlling the diameter of AuNPs in Au/rGOs. Furthermore, we selected 2 of the synthesized Au/rGOs, the weak ORR and OER catalysts, with specific Au particle sizes as the ideal anodic and cathodic promoters of $Ru(bpy)_3^{2+}$, and introduced them into a simple and eco-friendly potential-resolved ratiometric immunoassay for carcinoembryonic antigen (CEA) detection.

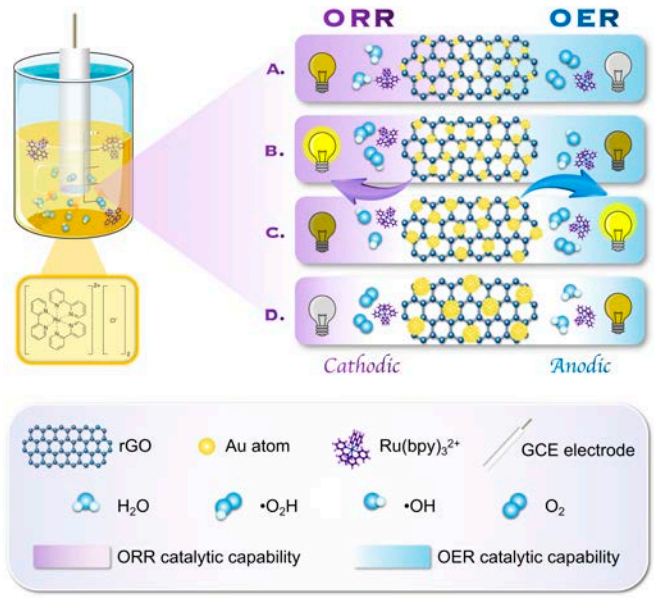


Fig. 1. A schematic illustration of the conversion of anodic and cathodic luminescence of $Ru(bpy)_3^{2+}$ by regulating the particle size of AuNPs in Au/rGO with corresponding ORR/OER catalytic performance.

Results and Discussion

Oxygen effect on the Au/rGO's regulation of $Ru(bpy)_3^{2+}$ luminescence

ORR catalytic effect of Au/rGO on $Ru(bpy)_3^{2+}$ cathodic luminescence

The final product of the ORR is water, but higher $Ru(bpy)_3^{2+}$ cathodic ECL demands more ROS. Therefore, an appropriate luminescence accelerator should be an ORR catalyst that can generate adequate ROS and prevent a full reaction from generating excessive water. Fortunately, ORR catalyst Au/rGO has an adjustable catalytic performance that can be enhanced by downsizing AuNPs and vice versa [13]. Meanwhile, the d-band theory indicates that larger AuNPs possess higher d-band center positions because more of their surface atoms have low coordination numbers, making it easier for intermediates to break off the surface and increase ROS generation [23]. Hence, Au/rGO with medium AuNPs size should have the greatest effect on promoting $Ru(bpy)_3^{2+}$ cathodic ECL, as it not only has the capacity to rapidly catalyze O_2 reduction but it also can result in the retention of more ROS products. Therefore, we synthesized a series of Au/rGO with the diameter of AuNPs gradually increased from 3 to 30 nm as the concentration of ydrogen tetrachloroaurate trihydrate ($HAuCl_4$) increased from 30 to 300 mM (Fig. 2) [24]. As shown in Fig. 3A, a relatively strong cathodic luminescence of $Ru(bpy)_3^{2+}$ reacting with Au/rGO-1 (minimal diameter (3.1 nm) of AuNPs) was observed at −1.7 V. Au/rGO-2 with medium-sized AuNPs (3.4 nm) promoted a super strong cathodic ECL of $Ru(bpy)_3^{2+}$, which is higher than the corresponding

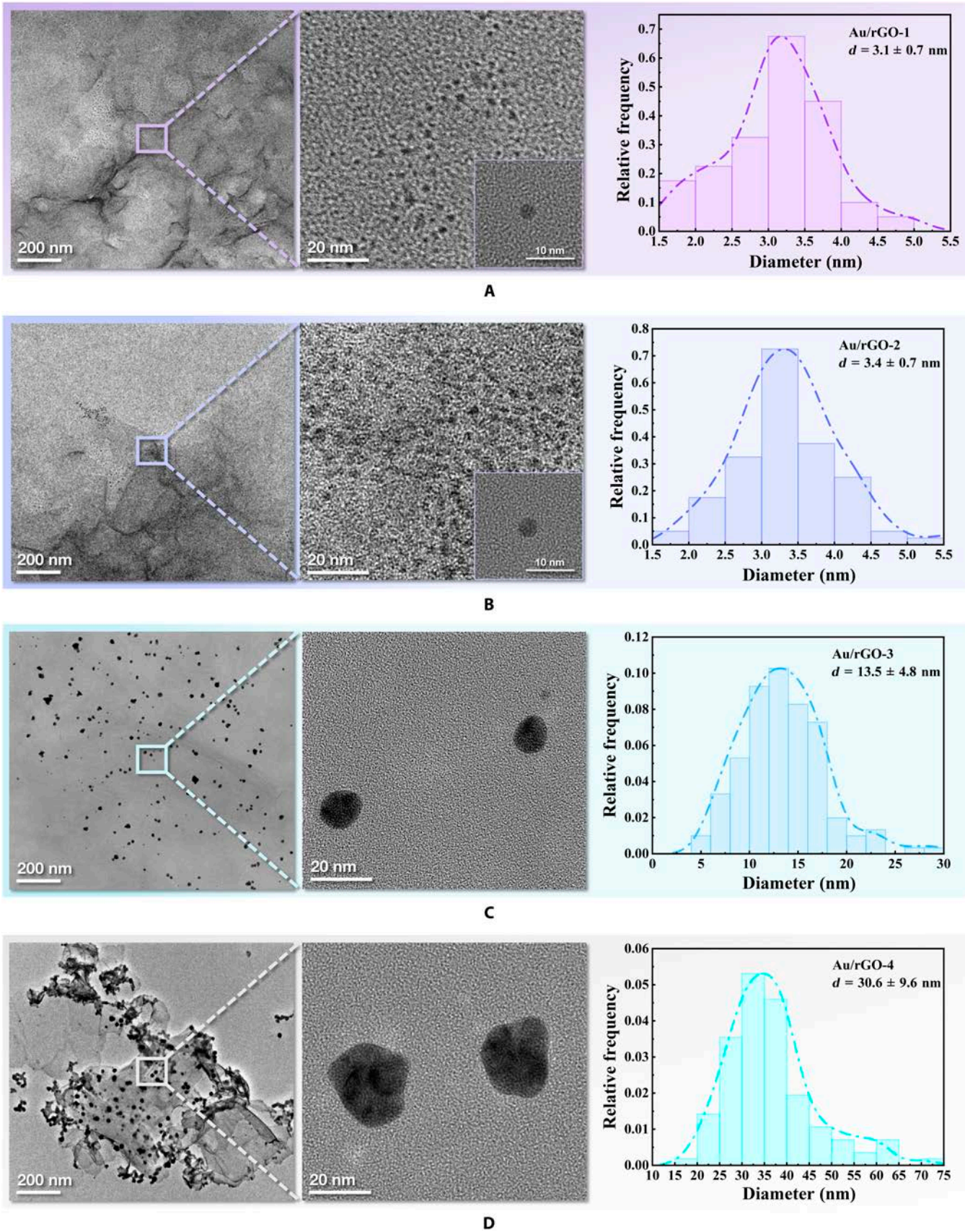


Fig. 2. The characteristics of the particle size of Au/rGOs. Transmission electron microscopy image and the corresponding size histograms of (A) Au/rGO-1, (B) Au/rGO-2, (C) Au/rGO-3, and (D) Au/rGO-4.

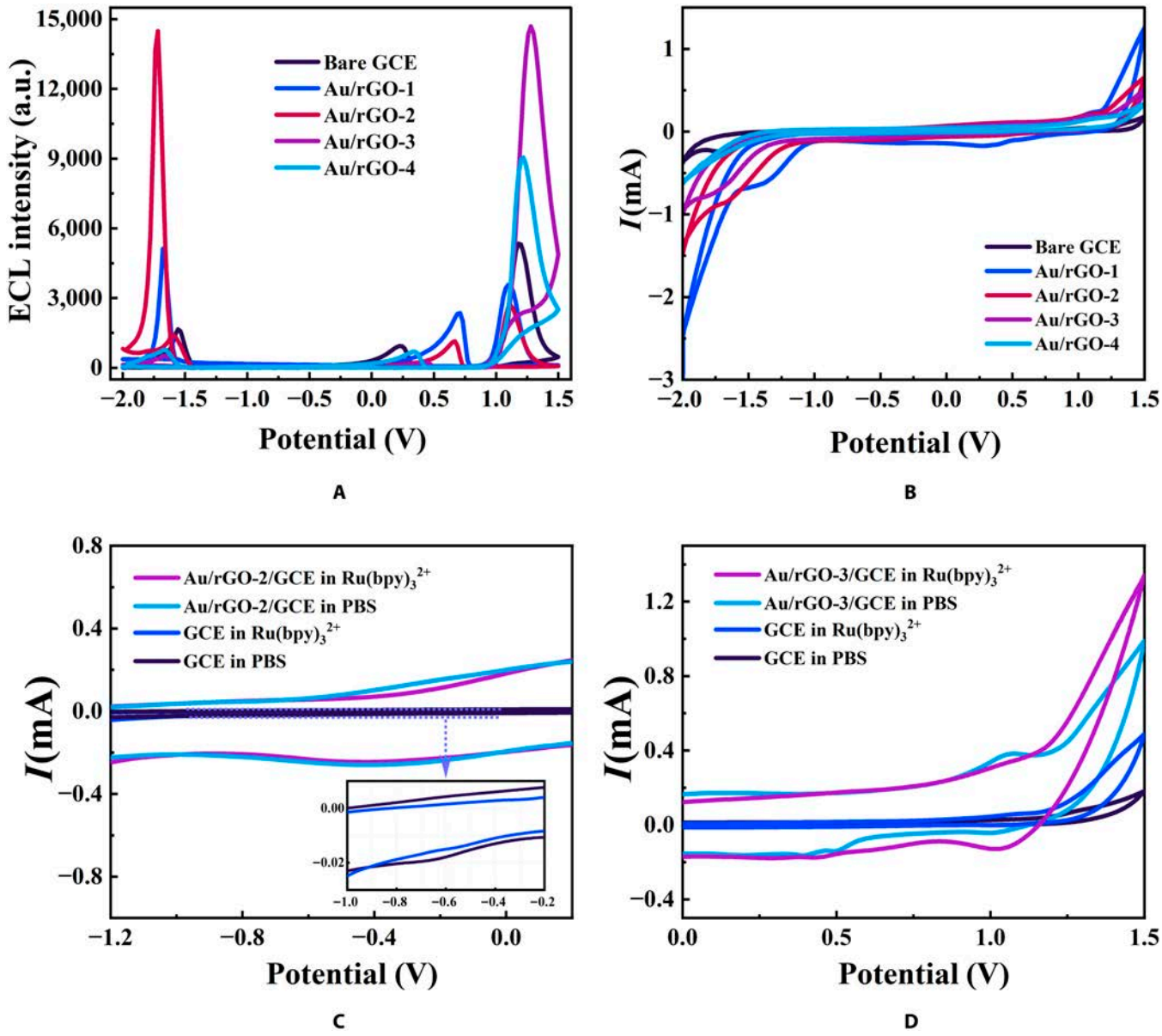


Fig. 3. The CV and ECL performance of Au/rGOs. The comparison of (A) ECL and (B) CV performance of Au/rGO-1, Au/rGO-2, Au/rGO-3, and Au/rGO-4. a.u., arbitrary units. The comparison of the CV performance of Au/rGO-2 (C) and Au/rGO-3 (D) on GCE in $Ru(bpy)_3^{2+}$ (purple line) and PBS (light blue line) as well as bare GCE in $Ru(bpy)_3^{2+}$ (dark blue line) and PBS (black line) at a scan rate of 0.1 V/s.

peak of Au/rGO-1. The cathodic peaks of $Ru(bpy)_3^{2+}$ with the large- (13 nm) and maximal-sized (30 nm) AuNPs loaded on rGO (Au/rGO-3 and Au/rGO-4) were even lower than with a bare glassy carbon electrode (GCE). Therefore, the ECL result verified that Au/rGO exhibited robust cathodic co-reactant characteristics of $Ru(bpy)_3^{2+}$ at intermediate AuNP particle sizes.

Cyclic voltammograms (CVs) were recorded to investigate the electrode reactions occurring in the potential scan range. Except for the reversible wave of the oxidation–reduction reaction of $Ru(bpy)_3^{2+}$ (1.13 and 1.05 V) and the reduction–oxidation reaction of $Ru(bpy)_3^{2+}$ (−1.65 and −1.60 V) (Fig. 3B), the small peak at −0.65 V observed on GCE in phosphate-buffered saline (PBS) and $Ru(bpy)_3^{2+}$/PBS is attributed to the ORR (inset in Fig. 3C). The peak is greatly increased and redshifted to −0.4 V after the embellishment of Au/rGO-2 on GCE, which indicates its catalytic performance in the ORR process (Fig. 3C).

CV curve of oxygen reduction for series of Au/rGOs are recorded in O_2-, air-, or N_2-saturated 0.1 M KOH aqueous solutions to validate the existence of the ORR process and compare their catalytic capabilities. As shown in Fig. 4B, the ORR onset potential is around −0.20 V (versus Ag/AgCl) with a reduction peak around −0.35 V (versus Ag/AgCl), which is consistent with the findings of Yin et al. [25]. The inhibition and enhancement of the reduction peak in N_2 and O_2 atmospheres illustrate the participation of oxygen in the reaction, which confirms the ORR process (Fig. 4A to C). The adjustable catalytic performance of Au/rGO is exhibited under the same atmosphere by CV (Fig. 4A to C) and linear sweep voltammetry (LSV) (Fig. S8). Specifically, Au/rGO-1 with the smallest AuNP particle size exhibits the best ORR catalytic performance, while as the particle size increased, Au/rGO's ORR catalytic ability deteriorated. The regulation of Au/rGO's ORR catalytic activity

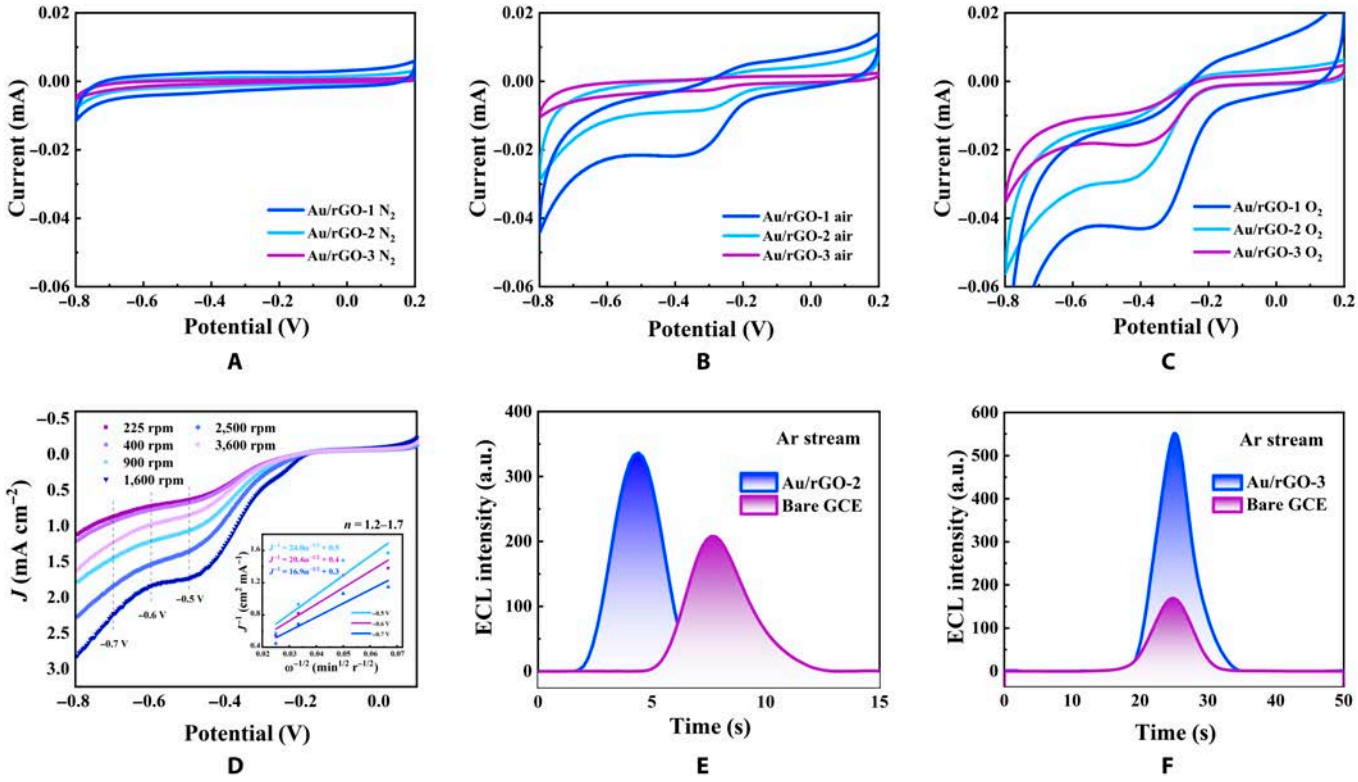


Fig. 4. The ORR catalytic performance and the co-reactant capacity of the Au/rGOs. The comparison of the CV lines of Au/rGO-1 (dark blue line), Au/rGO-2 (light blue line), and Au/rGO-3 (purple line) on GCE in (A) N_2-, (B) air-, and (C) O_2-saturated 0.1 M KOH. (D) RDE lines of Au/rGO-2 in O_2-saturated 0.1 M KOH at various rotation rates (ω) ranging from 225 to 3,600 rpm. Inset presents the K–L plots derived from the RDE measurements. All the scanning rates were 50 mV/s. ECL lines of bare GCE and Au/rGO-2 (−1.7 to −1.8 V versus Ag wire, scan rate of 0.1 V/s) (E) and Au/rGO-3 (F) in 1 mM $Ru(bpy)_3^{2+}$ acetonitrile solution (1.25 to 1.5 V versus Ag wire, scan rate of 0.1 V/s).

by varying AuNP's particle size may be attributed to the fact that smaller in situ growth of AuNPs on the rGO has less coordination, resulting in reduced electrophilicity of AuNPs, which decreases the activation energy of dissociative chemisorption of O_2 on AuNPs, further facilitating the O_2 reduction reaction and gaining [26]. It is proved by LSV that other noble metal NP (Ag and Pt)/rGO can also catalyze ORR (Fig. S9A). Among these, Au/rGO possesses the most potent properties for promoting $Ru(bpy)_3^{2+}$'s cathodic luminescence (Fig. S9B).

The oxygen reduction electron number was calculated on the basis of the LSV curves recorded on a rotating disk electrode (RDE) at different rotation rates (ω) to further clarify the major reaction process and products of the Au/rGO-2-catalyzed ORR reaction (Fig. 4D). The inset of Fig. 4D shows the Koutecky–Levich (K–L) plots (J^{-1} versus $\omega^{-1/2}$) at various electrode potentials. Calculated by the K–L equation [27], the transferred electron number (n) per oxygen molecule catalyzed by Au/rGO-2 is derived to be 1.2 to 1.7 across the potential range of −0.5 to −0.7 V. This result demonstrates that the 1-electron and 2-electron processes dominate O_2's reduction on Au/rGO-2, and the precise ROS produced by the ORR process is primarily $O^{2-\bullet}$ and H_2O_2, which play the dominant role in enhancing the cathodic ECL of $Ru(bpy)_3^{2+}$.

OER catalytic effect of Au/rGO on $Ru(bpy)_3^{2+}$ anodic luminescence

In the anodic ECL of $Ru(bpy)_3^{2+}$, O_2-related reactions are also involved. As mentioned in many reports, •OH plays an important role in promoting the anodic luminescence of $Ru(bpy)_3^{2+}$ [28]. Additionally, oxygen has been reported to be toxic to anodic ECL because it can quench the excited-state $Ru(bpy)_3^{2+}$ to undergo the non-radiation pathway [12]. Therefore, the superiority of Au/rGOs as a controlled $Ru(bpy)_3^{2+}$ cathode or anode accelerator is better highlighted by the fact that they likewise exhibit OER catalytic activity and the same meso-size-adjustable OER catalytic capacity, where the OER catalytic performance of Au/rGO increases as the AuNPs particle size decreases [29]. Given that the result of the OER reaction is oxygen, a suitable anode promoter should not only catalyze the loss of one electron from H_2O to create a high quantity of •OH but also avoid excessive O_2 generation. Therefore, a weaker catalyst for the OER reaction is required to shift the reaction toward Eq. 1 rather than Eq. 2. Moreover, considering the d-band theory, Au/rGO with larger particle-size AuNPs is expected.

$$H_2O - e^- \rightarrow HO\bullet + H^+ \quad (1)$$

$$O_2{}^- - e^- \rightarrow O_2 \quad (2)$$

As shown in Figs. 2C and D and 3A, the anodic ECL of $Ru(bpy)_3^{2+}$ at 1.1 V is substantially amplified when Au/rGO-3 and Au/rGO-4 with medium-large-sized (13 nm) and maximum (30 nm) AuNPs is loaded on the electrode. In addition, the anodic ECL of $Ru(bpy)_3^{2+}$ with Au/rGO-1 or Au/rGO-2 is weaker than that of the bare GCE, which can be due to the quenching effect of the OER-produced O_2. The anodic ECL of $Ru(bpy)_3^{2+}$ with Au/rGO-3 is superior to that of Au/rGO-4 because the OER catalytic capability of Au/rGO-4 with too large AuNP particle size is extremely weak to create sufficient

•OH, as shown in the CV diagram (Fig. 3D). Under anodic scanning of the bare GCE in $Ru(bpy)_3^{2+}$ solution, the CV current increased from the background current at 1.0 V owing to the oxidation of $Ru(bpy)_3^{2+}$, then grew more quickly because of the oxidation of water, and reached its peak at 1.5 V. The peak current value at 1.5 V was appropriately regarded as a symbol of OER degree because the oxidation of $Ru(bpy)_3^{2+}$ was supposed to result in a potential mass depletion of $Ru(bpy)_3^{2+}$ close to the electrode, and the shape of the summit current line at 1.5 V resembled a typical OER current [30]. In accordance with this notion, we employed CV to assess the OER catalytic performance of a series of synthesized Au/rGO catalysts. Figure 3B demonstrates that the OER catalytic capacity of Au/rGO-1 to Au/rGO-4 progressively decreased. This result confirm our inference that the anodic accelerator Au/rGO-3 with medium and weak OER catalytic properties can delay the OER reaction, prolonging the period during which the product •OH remains on the surface of the catalyst. Furthermore, the larger particle size of AuNPs allows •OH to have a greater propensity to desorb from Au/rGO-3, resulting in the accumulation of many •OH radicals in the vicinity of the electrode, which is conducive to strong ECL.

To confirm whether the ECL performance of $Ru(bpy)_3^{2+}$ modulated by altering the AuNP particle size of Au/rGOs was due to variable ORR and OER catalysis, we characterized the ECL enhancement effect of cathodic and anodic Au/rGOs under N_2 and O_2 atmospheres. As illustrated in Fig. S10A, the promotion effect of the cathode promoter Au/rGO-2 on (blue line) $Ru(bpy)_3^{2+}$ cathodic ECL was diminished in the N_2 environment owing to the removal of dissolved oxygen in the system by N_2, which inhibited the occurrence of ORR reactions. The enhancement of anodic luminescence was due to the disappearance of the quenching effect of dissolved oxygen on $Ru(bpy)_3^{2+*}$. By contrast, the ORR process was stimulated in an O_2 environment (black line), resulting in increased $Ru(bpy)_3^{2+}$ cathodic ECL. Figure S10B shows the influence of the anode promoter Au/rGO-3 on the luminescence of $Ru(bpy)_3^{2+}$ in various atmospheres. Under N_2 atmosphere (black line), the anode luminescence of $Ru(bpy)_3^{2+}$ was remarkably enhanced. This finding may be attributed to the fact that the Au/rGO-3-catalyzed OER reaction produces the intermediate product •OH and other ROS to promote anode luminescence, whereas the by-products O_2 and dissolved O_2 are removed by the N_2 gas stream. The anodoluminescence of $Ru(bpy)_3^{2+}$ was remarkably diminished, and the cathodic ECL was barely enhanced after the introduction of O_2. This finding is because Au/rGO-3 lacks a potent ORR catalytic capacity, and the increased dissolved O_2 in the electrolyte has a strong quenching effect on the anodic luminescence of $Ru(bpy)_3^{2+}$. The preceding results demonstrate that the ORR catalytic capacity of Au/rGO-2 can affect in promoting $Ru(bpy)_3^{2+}$ cathodic ECL, whereas dissolved O_2 in the solution and O_2 created by the OER reaction on the electrode surface suppress $Ru(bpy)_3^{2+}$ anode luminescence. However, the exact components produced by the Au/rGO-2 catalytic ORR that promote $Ru(bpy)_3^{2+}$ cathodic ECL, as well as the independent role of •OH or other ROS components produced by Au/rGO-3 catalyzing OER that contribute to $Ru(bpy)_3^{2+}$ anodic luminescence, remain unknown. Therefore, we introduced superoxide dismutase (SOD) and isopropanol, inhibitors of •OH, as well as benzoquinone (BQ), inhibitor of $O^{2-\bullet}$, to independently reflect the effects of various catalyzed ROS components on $Ru(bpy)_3^{2+}$ cathodic and anodic luminescence. The results are shown in Fig. S11: SOD and isopropanol can reduce the Au/rGO-2-promoted cathodic ECL by approximately 55% and 90%, respectively, and BQ can reduce it by about 99%, indicating that Au/rGO-2 mainly fosters $Ru(bpy)_3^{2+}$'s cathodic ECL by catalyzing O_2 reduction to $O^{2-\bullet}$, which is consistent with the results of the electron transfer number calculated by the K–L equation. For the anodic promoter Au/rGO-3 modified on the electrode, the anodic luminescence of $Ru(bpy)_3^{2+}$ decreased by approximately 20% when BQ was added, whereas SOD and isopropanol suppressed the anodic luminescence by about 50% and 70%, respectively, confirming that Au/rGO-3 was successfully manufactured as a weak OER catalyst, thereby implementing the concept of creating •OH as the primary OER product on the electrode surface to promote anodic luminescence.

Co-reactant and other pathways for Au/rGO's promotion of $Ru(bpy)_3^{2+}$ luminescence

Given the versatile properties of rGO, such as good catalytic ability, excellent electrical conductivity, and an abundance of functional groups [31], other mechanisms for rGO promoting $Ru(bpy)_3^{2+}$ luminescence should be investigated. For instance, rGO can participate in the co-reactant luminescence pathway of $Ru(bpy)_3^{2+}$ by leveraging its hydroxyl, epoxy, carbonyl, and carboxyl functional groups. Alternatively, rGO can directly promote luminescence by increasing the electron transfer efficiency of the reaction.

Acetonitrile was chosen as the appropriate ECL solvent to evaluate the co-reactant performance of Au/rGO, allowing all ORR and OER reactions involving O_2, dissolved O_2, and O atoms in H_2O to be avoided [12]. The results are shown in Fig. 4E and F. In comparison to an empty GCE, the electrode modified with Au/rGO-2 has a weak promotion effect on $Ru(bpy)_3^{2+}$ cathodic ECL, whereas Au/rGO-3 can remarkably promote $Ru(bpy)_3^{2+}$ anode emission, which indicates that there could be other pathways for Au/rGO-3 to promote $Ru(bpy)_3^{2+}$ emission.

To further identify whether the mechanism of Au/rGO-3's oxygen-free participation in $Ru(bpy)_3^{2+}$ anodic luminescence promoting is through direct catalysis or co-reactant pathway, we performed CV detection of Au/rGO-3 in PBS. The CV diagram in Fig. 3D exhibits a substantial reduction peak at 1.1 V, which may be attributed to the oxygen-containing groups (carboxyl and hydroxyl groups) on the surface of rGO directly gaining and losing electrons with the electrode, indicating that Au/rGO-3 may act as a co-reactant to undergo reduction–oxidation and oxidation–reduction reactions with $Ru(bpy)_3^{2+}$. Three tiny redox peaks emerging at 0.3, 0.4, and 0.5 V can be attributed to the electrode reduction of AuNPs. The anode peak of $Ru(bpy)_3^{2+}$ shifted to the left after the modification of Au/rGO-3 on the electrode, implying that Au/rGO-3 can perform as a catalyst to accelerate the electron transfer of $Ru(bpy)_3^{2+}$ [32].

In the process of •OH enhancing $Ru(bpy)_3^{2+}$'s anodic luminescence, Au/rGO-3 acts as an OER catalyst and provides the carboxyl group to promote $Ru(bpy)_3^{2+}$'s luminescence through the co-reactant pathway simultaneously. Carboxylic acid might be oxidized by the electrogenerated •OH to yield strong reducing intermediates $CO_2^{-\bullet}$ that can function as a co-reactant and react with $Ru(bpy)_3^{3+}$ to emit light [28]. When Au/rGO-3 was electrochemically reduced at −1.0 V for 20 min on GCE, the

anodic ECL fell remarkably, indicating that oxygenated groups are required for the anodic ECL (Figure S12). The reduction in the fraction of oxygen atoms after Au/rGO-3/GCE reacted with $Ru(bpy)_3^{2+}$ confirmed the aforesaid result (Fig. S13). Therefore, Au/rGO-3-catalyzed OER reaction to improve anodic luminescence is essentially achieved by accelerating the co-reaction reaction between $Ru(bpy)_3^{2+}$ and carboxyl groups under the anodic scan.

Possible ECL mechanism of Au/rGOs regulating the conversion of the dual-potential ECL of $Ru(bpy)_3^{2+}$

To determine how AuNPs, GO, and rGO interact with $Ru(bpy)_3^{2+}$, we examined the co-reactant characteristics of AuNPs, GO, rGO, and their combinations in a $Ru(bpy)_3^{2+}$ solution. As shown in Fig. S14A, AuNPs with smaller particle sizes demonstrated a superior cathode promotion effect because of their preferable ORR electrocatalytic activity. This is because smaller AuNPs have more surface atoms that can absorb and activate O_2 molecules than larger AuNPs [33]. Moreover, the degree of rGO reduction also has an impact on its co-reactant properties. As shown in Fig. S14B, GO possesses a certain anodic stimulation property that can be altered after the reduction of rGO by hydrazine hydrate, which has a greater cathodic ECL promotion capacity than GO. Considering that the elemental ratio characterized by x-ray photoelectron spectroscopy (XPS) shows a much lower ratio of NH_2^- (2.68% of N1s) than oxygen-containing functional groups (28.16% of O1s; Table S2), the moderately poor anodic co-reactant property of rGO may be due to the anode promotion functions of amino groups on rGO being less significant, than the anodic luminescence degradation effect caused by the reduction of oxygen-containing functional groups. The effect of the degree of rGO reduction on the co-reactant performance of Au/rGO was further investigated by measuring the ratio of the cathodic and anodic luminescence (I_c/I_a) of $Ru(bpy)_3^{2+}$ co-reacted with various Au/rGO under different rGO reduction times. As shown in Fig. S15, the redshift of the ultraviolet-visible spectra indicates an increasing reduction degree of rGO, and $lg(I_c/I_a)$ reaches its maximum at a reduction time of 6 h before decreasing with the extension of the reduction time. The optimum I_c/I_a of $Ru(bpy)_3^{2+}$ catalyzed by Au/rGO with partially reduced rGO can be attributed to the fact that the defective graphene substrate formed by the incomplete reduction reaction can accelerate charge transfer from AuNPs to O_2, which lowers the energy barrier of the rate-limiting steps by destabilizing the intermediate species of ORR and decreasing the dissociation activation energy of O_2, leading to increased ROS production [34]. However, the presence of either Au or rGO alone had a remarkably lower promoting effect on the $Ru(bpy)_3^{2+}$ cathode and anode luminescence than the 2 combinations, showing that the Au/rGO complex exerts its co-reactant feature through the interaction of Au and rGO as a whole (Fig. S14). This finding can be explained by few possible reasons, one of which is that the hybridization enhances the stability of AuNPs. Another potential explanation is that hybridizing AuNPs with rGO at graphene defects enhances their ORR catalytic activity by increasing charge transfer from the metal to the substrates.

On the basis of the discussed results, the principle of cathodic luminescence has been clarified clearly (Scheme S1). As Au/rGO-2 primarily catalyzes the $1e^-$ to $2e^-$ ORR, the major reactants in $Ru(bpy)_3^{2+}$'s cathodic luminescence are $\bullet O_2H$ and H_2O_2, according to the electron transfer number (n) calculated using the K–L equation. Therefore, for the cathodic ECL reaction, $Ru(bpy)_3^{2+}$ is initially reduced at negative potentials to transform into $Ru(bpy)_3^{+}$. Then, the highly oxidative $\bullet O_2H$ may directly oxidize $Ru(bpy)_3^{+}$ to $Ru(bpy)_3^{2+*}$ or oxidize Au/rGO to generate $[Au/rGO]_{ox}^{\bullet}$, which indirectly oxidize $Ru(bpy)_3^{+}$ (pathway 1). Meanwhile, H_2O_2 can be electro-reduced to $\bullet OH$, which also possesses strong oxidation properties. Similarly, $\bullet OH$ can oxidize $Ru(bpy)_3^{2+}$ to create a high-energy $Ru(bpy)_3^{2+*}$ state, thereby triggering cathode luminescence (pathway 2). Given that ROS has high oxidation potentials, $\bullet O_2H$ and $\bullet OH$ may directly oxidize $Ru(bpy)_3^{2+}$ to create $Ru(bpy)_3^{3+}$, which can then react with $Ru(bpy)_3^{+}$ to release light via an annihilation reaction (pathway 3).

$$Ru(bpy)_3^{2+} + e^- \rightarrow Ru(bpy)_3^{+} \quad (3)$$

Pathway 1:

$$O_2 + e^- + H^+ \rightarrow \bullet O_2H \quad (4)$$

$$Ru(bpy)_3^{+} + \bullet O_2H + H^+ \rightarrow Ru(bpy)_3^{2+*} + H_2O_2 \rightarrow Ru(bpy)_3^{2+} + h\nu \quad (5)$$

$$Au/rGO + \bullet O_2H \rightarrow [Au/rGO]_{ox}^{\bullet} + H_2O_2 \quad (6)$$

$$Ru(bpy)_3^{+} + [Au/rGO]_{ox}^{\bullet} + H^+ \rightarrow Ru(bpy)_3^{2+*} + Au/rGO \rightarrow Ru(bpy)_3^{2+} + h\nu \quad (7)$$

Pathway 2:

$$H_2O_2 + H^+ + e^- \rightarrow H_2O + \bullet OH \quad (8)$$

$$Ru(bpy)_3^{+} + \bullet OH + H^+ \rightarrow Ru(bpy)_3^{2+*} + H_2O \rightarrow Ru(bpy)_3^{2+} + h\nu \quad (9)$$

$$Au/rGO + \bullet OH \rightarrow [Au/rGO]_{ox}^{\bullet} + H_2O \quad (10)$$

$$Ru(bpy)_3^{+} + [Au/rGO]_{ox}^{\bullet} + H^+ \rightarrow Ru(bpy)_3^{2+*} + Au/rGO \rightarrow Ru(bpy)_3^{2+} + h\nu \quad (11)$$

Pathway 3:

$$Ru(bpy)_3^{2+} + \bullet O_2H + H^+ \rightarrow Ru(bpy)_3^{3+} + H_2O_2 \quad (12)$$

$$Ru(bpy)_3^{2+} + \bullet OH + H^+ \rightarrow Ru(bpy)_3^{3+} + H_2O \quad (13)$$

$$Ru(bpy)_3^{+} + Ru(bpy)_3^{3+} \rightarrow Ru(bpy)_3^{2+*} + Ru(bpy)_3^{2+} \rightarrow Ru(bpy)_3^{2+} + h\nu \quad (14)$$

Because of the high oxidation potential of $\bullet O_2H$ ($E°(\bullet O_2H/H_2O_2)$ = 1.51 V versus SHE), $\bullet O_2H$ is a sufficiently robust

oxidizing agent to convert $Ru(bpy)_3^{+}$ into $Ru(bpy)_3^{2+*}$. To validate this feature, we used the following equation to calculate the energy ($-\Delta H°$) accessible in Eq. 5.

$$-\Delta H° \approx E°\left(\bullet O_2H/H_2O_2\right) - E°\left(Ru(bpy)_3^{1+/2+}\right) - 0.1\ eV \tag{15}$$

in which $E\ (Ru(bpy)_3^{1+/2+}) = -1.41$ V versus SHE, and 0.1 eV is an estimate of the entropy term ($T\Delta S°$) at 25 °C. $-\Delta H°$ is calculated to be 2.82 eV, and the energy required to produce $Ru(bpy)_3^{2+*}$ is 2.12 eV, indicating that the reaction has sufficient energy to produce $Ru(bpy)_3^{2+*}$, making Eq. 5 an energy-rich system. Given that the hydroxyl radical (•OH) has a higher oxidation potential ($E°(H_2O_2/\bullet OH) = 1.77$–$1.91$ V versus SHE) than $\bullet O_2H$, the enthalpy of reaction Eq. 9 is at least 2.95 V (2.95 to 3.09 eV), making Eq. 9 theoretically possible.

For anode reactions, Au/rGO-3 can be employed as a co-reactant and an OER catalyst to enhance the luminescence of $Ru(bpy)_3^{2+}$. As the anodic co-reactant, Au/rGO-3 reacts with $Ru(bpy)_3^{2+}$ mainly through its surface oxygen-containing groups (carboxyl and hydroxyl) and amino groups to convert $Ru(bpy)_3^{2+}$ to the excited state, during which the amino groups perform similarly to tripropylamine [10,35], and the hydroxyl groups functions mechanistically comparable to alcohols and its derivatives [28,36–38] as the anodic co-reactant of $Ru(bpy)_3^{2+}$. In addition, as a weak catalyst for the OER process, Au/rGO-3 may catalyze the oxidation of water to •OH. Then, •OH enhances the decarboxylation of Au/rGO-COO^- to yield Au/rGO•, which can transfer electrons to $Ru(bpy)_3^{3+}$ to produce $Ru(bpy)_3^{2+*}$. Moreover, the interaction of a small amount of •OH with Au/rGO-COO^- might create $CO_2^{-\bullet}$ with substantial reductivity, which can subsequently reduce $Ru(bpy)_3^{2+}$ to $Ru(bpy)_3^{+}$, followed by its interaction with $Ru(bpy)_3^{3+}$ in an annihilation-type luminescence process. Moreover, Au/rGO-3 could also accelerate the electron transfer as a catalyst to improve $Ru(bpy)_3^{2+}$'s luminescence efficiency. The specific equations are as follows:

$$Ru(bpy)_3^{2+} - e^- \rightarrow Ru(bpy)_3^{3+} \tag{16}$$

Pathway 1:

$$Au/rGO(ArCHOHR) - e^- \rightarrow [Au/rGO(ArCHOHR)]^{+\bullet} \rightarrow [Au/rGO(ArCOHR)]^{\bullet} \tag{17}$$

$$\left[Au/rGO(ArCOHR)\right]^{\bullet} + Ru(bpy)_3^{3+} \rightarrow Ru(bpy)_3^{2+*} + Au/rGO(ArCOR) \rightarrow Ru(bpy)_3^{2+} + h\nu \tag{18}$$

Pathway 2:

$$Au/rGO\left(ArNRCH_2R'\right) - e^- \rightarrow \left[Au/rGO\left(ArNRCH_2R'\right)\right]^{+\bullet} \tag{19}$$

$$\left[Au/rGO\left(ArNRCH_2R'\right)\right]^{+\bullet} - H^+ \rightarrow \left[Au/rGO\left(ArNRCHR'\right)\right]^{\bullet} \tag{20}$$

$$\left[Au/rGO\left(ArNRCHR'\right)\right]^{\bullet} + Ru(bpy)_3^{3+} \rightarrow \left[Au/rGO\left(ArN{=}CHR'\right)\right]^{+} + Ru(bpy)_3^{2+*} \rightarrow Ru(bpy)_3^{2+} + h\nu \tag{21}$$

$$\left[Au/rGO\left(ArN{=}CHR'\right)\right]^{+} + H_2O - H^+ \rightarrow Au/rGO(ArNRH) + R'CHO \tag{22}$$

Pathway 3:

$$H_2O - e^- \rightarrow H^+ + \bullet OH \tag{23}$$

$$Au/rGO - COO^- + \bullet OH + H^+ \rightarrow Au/rGO - COO^{\bullet} + H_2O \rightarrow Au/rGO^{\bullet} + CO_2 + H_2O \tag{24}$$

$$Ru(bpy)_3^{2+} - e^- \rightarrow Ru(bpy)_3^{3+} \tag{25}$$

$$Au/rGO^{\bullet} + Ru(bpy)_3^{3+} \rightarrow Au/rGO^{+} + Ru(bpy)_3^{2+*} \rightarrow Ru(bpy)_3^{2+} + h\nu \tag{26}$$

Therefore, the transformation of Au/rGO from $Ru(bpy)_3^{2+}$'s anodic promoter to its cathodic promoter by increasing the particle size of AuNPs may be due to the following reasons. First, with the increase in the particle size of AuNPs, the capability of Au/rGO to catalyze the ORR and OER gradually decreases, resulting in an insufficient production of ROS, which weakens cathodic luminescence. Meanwhile, a relatively high ratio of •OH to O_2 is produced in the OER process, which facilitates the anodic process. Second, with the increase in the size of the single AuNP particles covalently bonded on the surface of rGO, the distribution density of AuNPs decreased, thereby diminishing their masking effect on the reactive sites of the anodic co-reactants (amino groups, oxygen-containing groups, etc.) on the surface of rGO, leading to an enhancement of anodic luminescence.

Construction and characterization of the single luminophore ratiometric ECL sandwich immunoassay

Ratiometric ECL assays have been widely applied in biosensing because they can provide more accurate results in complex environments by eliminating background signals and interferences through the self-calibration of the 2 emissions [39]. Although many reported ratiometric ECL systems based on ECL-resonance energy transfer (ECL-RET), competitive strategies, or enzymatic reactions have provided reliable and sensitive sensing signals, they mainly require 2 elaborately picked potential-resolved luminophores and complex combinations of co-reactants. Moreover, the multiple assembly steps and labeling courses could cause the chemical cross talk or energy transmission between ECL materials. Additionally, the existing single luminophore system has limited detection sensitivity for label-free construction models and unidirectional signal change output (Fig. 5A and B). Thus, if employing emission promoters rather than conventional luminophores as the substrate and label in an immunosensor and with the luminophore in the electrolyte, then the platform can be substantially simplified by utilizing the potential-resolved single-luminophore ECL system.

Therefore, we selected the most favorable cathodic and anodic promoters Au/rGO-2 and Au/rGO-3 to modify Ab_2 and GCE for the construction of immunosensor for CEA detection,

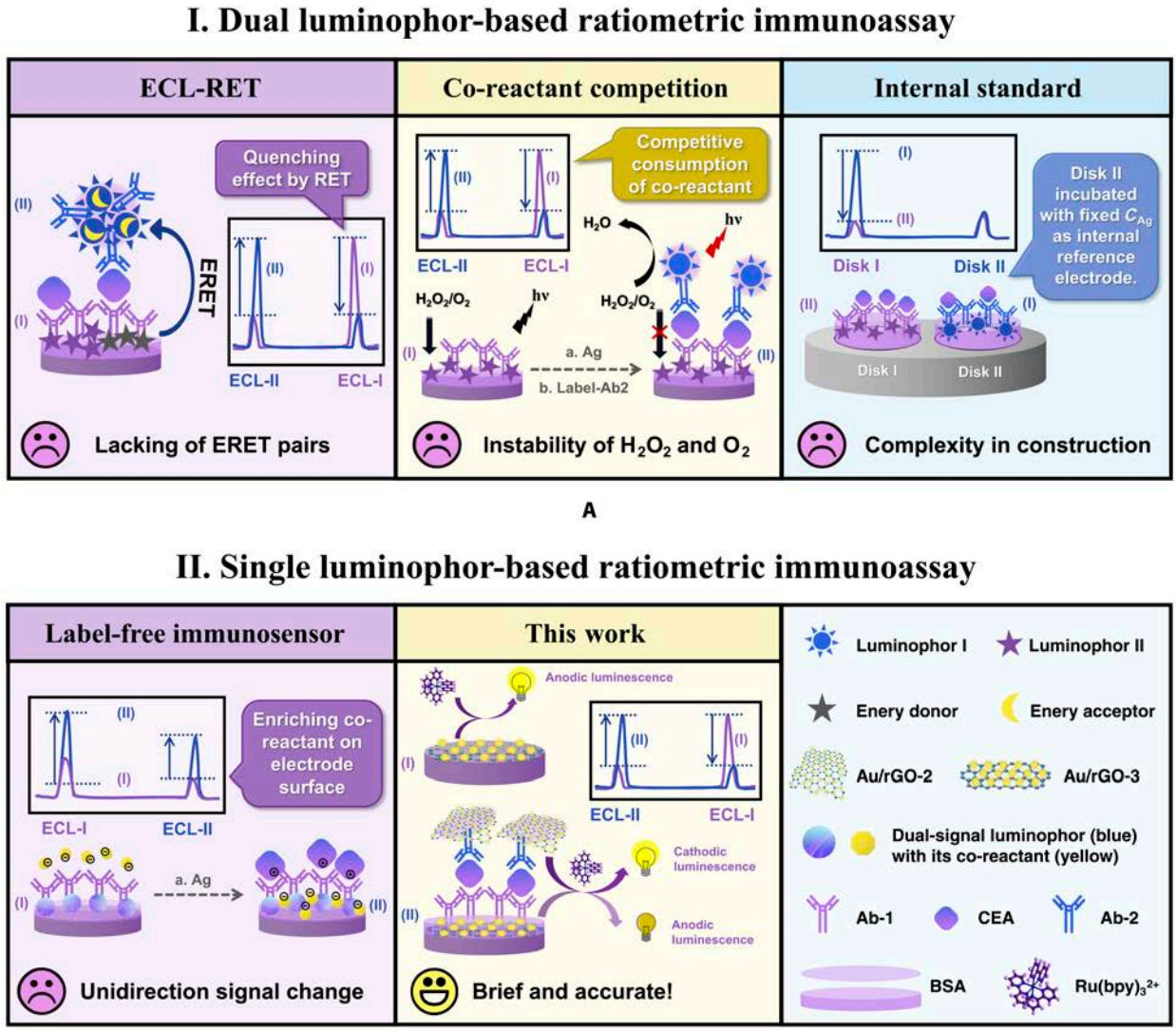


Fig. 5. The schematic illustrations of various construction strategies of ratiometric immunosensor and the construction of the potential-resolved single-luminophore ratiometric ECL immunoassay. (A) Traditional building strategies for ratiometric immunosensor are mostly based on dual luminophores with their corresponding co-reactant, such as the ECL-RET strategy, competitive co-reactant-consuming strategy, and internal standard strategy. ERET, electrochemiluminescence RET. (B) Single luminophore with potential-resolved dual signal is introduced for building the ratiometric immunoassay to simplify the platform, which is usually applied in the label-free immunosensor. In this work, we innovatively implied the anodic and cathodic co-reactants of $Ru(bpy)_3^{2+}$ to be the substrate and label of the sandwich immunosensor for competitive consumption of $Ru(bpy)_3^{2+}$ dissolved in the electrolyte, which achieved the bidirectional signal change and accurate detection in a simple system. EIS (C) and the enlarged picture from 0 to 500 Ω (D) of (I) bare GCEs, (II) Au/rGO-3/GCE, (III) BSA/anti-CEA-1/Au/rGO-3/GCE, (IV) CEA/BSA/anti-CEA-1/Au/rGO-3/GCE, and (V) anti-CEA-2/CEA/BSA/anti-CEA-1/Au/rGO-3/GCE. EIS was measured in 0.1 mol l^{-1} of KCl containing 5.0 mmol l^{-1} of $K_3[Fe(CN)_6]/K_4[Fe(CN)_6]$ (1:1). Rs, solution resistance; Cdl, double-layer capacitance; Rct, charge transfer resistance; Zw: Warburg impedance.

respectively. Electrochemical impedance spectroscopy (EIS) was conducted to track the stepwise assembly process of the electrode by using $[Fe(CN)_6]^{3-/4-}$ as the redox probe (Fig. 5C and D). Compared with the bare GCE (curve I), a smaller impedance value was observed for the Au/rGO-3-modified GCE (curve II) because of the good conductivity of rGO. The impedance values gradually increased after the electrode was assembled with Ab_1 and bovine serum albumin (BSA) (curve III), CEA (curve IV), and Au/rGO-2-Ab_2 bioconjugates (curve V) successively because the Ab_1 and BSA, CEA, and Au/rGO-2-Ab_2 bioconjugates acted as mass-transfer blocking layers that impeded electron transport. Importantly, these results indicated that the biosensor was successfully fabricated.

Optimization of detection conditions

The selection of optimal test conditions is particularly important to achieve excellent performance in the ECL CEA assay [40]. In this system, we optimized 3 necessary factors: pH, concentration ratio of Au/rGO-2 and Au/rGO-3 as the label and substrate of the immunosensor, and concentration of $Ru(bpy)_3^{2+}$ (Fig. S16). The optimal pH value of the detection environment was controlled at 6 because the ECL ratio of the cathode to the anode (I_c/I_a) of the Au/rGO-2/GCE-$Ru(bpy)_3^{2+}$ system reached the maximum under cathode scanning, and Au/rGO-3 showed the lowest I_c/I_a at pH 6 owing to the prominent emission under anodic scanning. This indicates that both the cathodic and anodic luminescence promoters perform optimally at pH 6.

The appropriate label-to-substrate concentration ratio in a ratiometric immunoassay can ensure that the cathode and anode signals of the ECL could clearly invert with a change in the antigen concentration of the ratiometric sensor. The Ab_2 tag Au/rGO-2 flips the anode-to-cathode signal with the increase in the antigen concentration by competing with the reaction of $Ru(bpy)_3^{2+}$ and Au/rGO-3 modified on the electrode. Therefore, if the concentration ratio of Au/rGO-2 to Au/rGO-3 is extremely low or high, then the ECL anode luminescence will be slow to change or the cathodic luminescence will always dominate, resulting in no significant change in the ratio of cathodic to anodic ECL intensity (I_c/I_a), which is disadvantageous to the detection sensitivity. Therefore, we optimized the Au/rGO-2-to-Au/rGO-3 ratio to 1:1 when the value of I_c/I_a reached its apex. Concurrently, I_c/I_a attained its maximum value at a $Ru(bpy)_3^{2+}$ concentration of approximately 1 mM. When an excess of $Ru(bpy)_3^{2+}$ was present in the solution, the addition of Au/rGO-2 had a minimal effect on the reaction of Au/rGO-3 with $Ru(bpy)_3^{2+}$, resulting in negligible inversion of the anode-to-cathode signal with the increase in the antigen concentration.

Analytical performance of the ratiometric ECL biosensor

With the increase in the CEA concentrations, the anodic intensity decreased, whereas the cathodic ECL intensity increased (Fig. 6A). Figure 6B demonstrates a strong linear association between the ECL intensity ratio of anodic-to-cathodic ECL intensity (I_c/I_a) and the logarithmic concentration of CEA in the range of 10^{-7} to 10^{-1} ng/ml. The regression equation was $lg(I_c/I_a) = 0.26lgC + 1.43$ with a correlation coefficient of $R^2 = 0.9995$. Therefore, the suggested ratiometric biosensor for the detection of CEA had an outstanding analytical performance and had a low limit of detection of 0.33 fg/ml (signal-to-noise ratio = 3), which was superior to other strategies indicated in Table S1. The comparison of Au/rGO-2 with some traditional $Ru(bpy)_3^{2+}$ cathodic co-reactants shows its excellent cathodic ECL promotion performance (Fig. S17).

Selectivity and stability

Different tumor markers (vascular endothelial growth factor receptor 2 (VEGFR2), estrogen receptor alpha (ERα), and nuclear matrix protein 22 (NMP22)) were used as interfering compounds at 10^{-2} ng/ml to evaluate the selectivity of the immunosensor. As shown in Fig. 6C, VEGFR2, ERα, and NMP22 have lower $lg(I_c/I_a)$ compared with CEA. Because the interference groups only have Ab_1 and no Ab_2, its anode emission is extremely strong, and its cathode emission is modest. The detection value of $lg(I_c/I_a)$ for a mixture of 10^{-4} ng/ml of CEA, 10^{-2} ng/ml of VEGFR2, 10^{-2} ng/ml of ERα, and 10^{-2} ng/ml of NMP22 is only slightly lower than 10^{-4} ng/ml of CEA, demonstrating the good selectivity of the proposed immunosensor. Figure 6D shows the stability of the ECL ratiometric approach at 10^{-5} ng/ml. The anodic and cathodic RSDs are 1.86% and 5.27%, respectively, indicating a robust biosensor stability.

Detection of CEA in real human serum samples

To evaluate the analytical reliability and potential applicability of the constructed ratiometric immunosensor for testing real samples, we collected 10 human serum specimens with various CEA concentrations from the Guizhou Provincial People's Hospital in accordance with the rules of the local ethical committee. Before measurement, serum samples were diluted appropriately in a stepwise manner to be within the linear range of the immune device using 0.01 M PBS and then monitored using the developed ECL immunoassay. The results were compared with those obtained using the commercialized ECLIA method (Electrochemiluminescent Analyzer, Roche E801, Switzerland). The results are listed in Table with the relative errors ranged from −7.54% to 9.25%. No significant difference was observed between the results obtained by 2 methods. Therefore, the ratiometric ECL biosensing system constructed in this work can be reasonably applied in the clinical determination of CEA in human plasma.

Conclusion

In this study, we proposed a simplified multisignal ECL system using only a single luminophore, $Ru(bpy)_3^{2+}$, and a similar co-reactant, Au/rGOs. The cathodic process of $Ru(bpy)_3^{2+}$ is related to the ROS produced in the ORR process, and the anodic process can be quenched by O_2 and enhanced by •OH, the final product and the intermediate product of the OER. We synthesized a series of Au/rGOs with different AuNP diameters to investigate the relationship between their ORR and OER activities and their effects on the luminescence of $Ru(bpy)_3^{2+}$. The results demonstrate that Au/rGO with medium- to small-sized AuNPs mainly fosters cathodic ECL of $Ru(bpy)_3^{2+}$ by catalyzing the ORR to produce ample ROS while avoiding the complete reaction that generates excessive water. The weak OER catalyzer, Au/rGO with medium-large AuNPs, showed an evident promotion effect on the anodic luminescence of $Ru(bpy)_3^{2+}$ by generating •OH as the

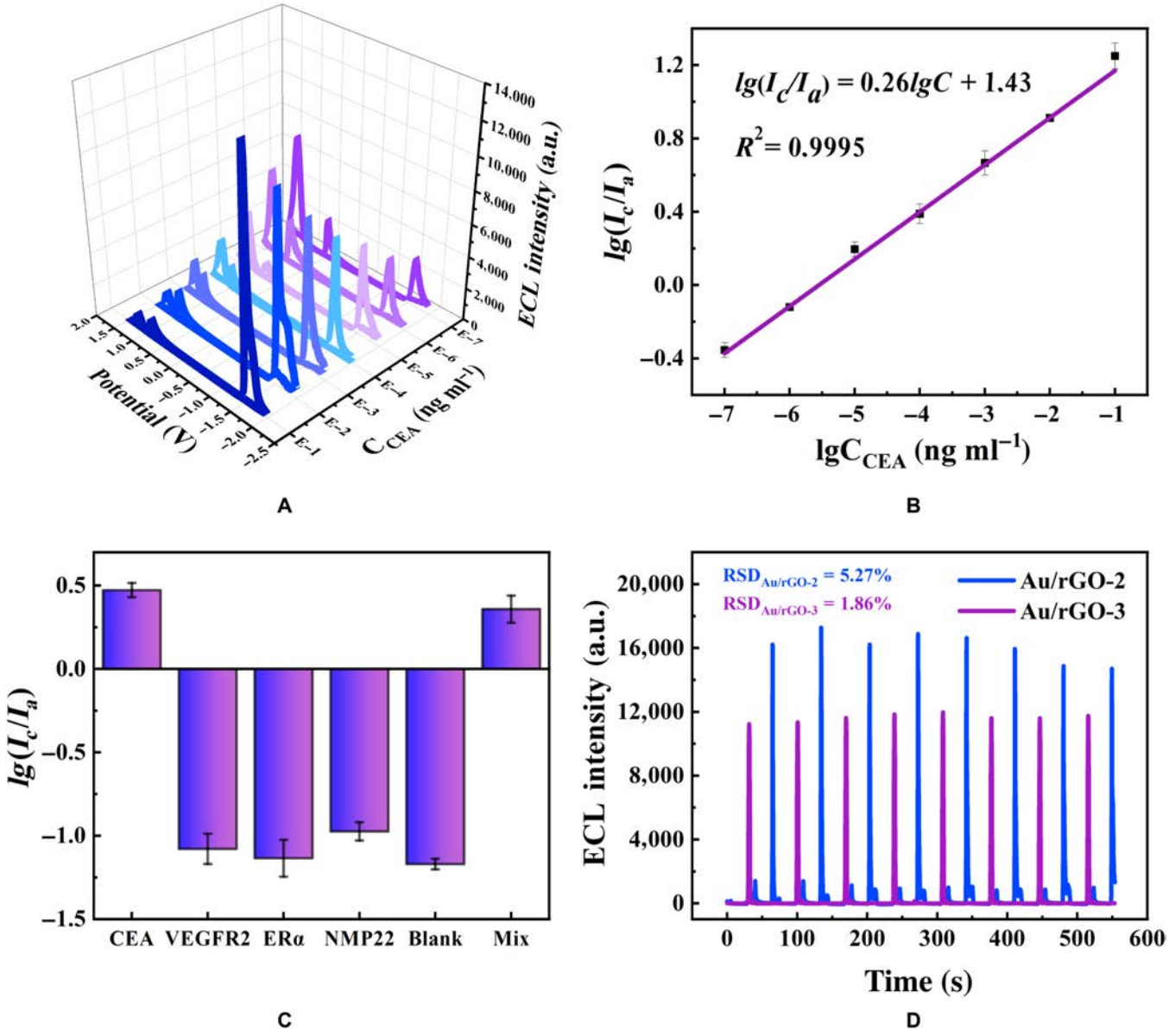


Fig. 6. Detection performance of the ratiometric ECL immunosensor. (A) ECL responses of the ratiometric biosensor and (B) calibration plot of the ECL intensity with different concentrations of CEA from 10^{-7} to 10^{-1} ng/ml in 1 mM $Ru(bpy)_3^{2+}$. (C) The selectivity of the proposed ratiometric ECL biosensor. (D) Stability of ECL emission of Au/rGO-2 (blue line) and Au/rGO-3 (purple line) in $Ru(bpy)_3^{2+}$ for the detection of 10^{-5} ng/ml of CEA

primary OER product and avoiding O_2. This work solved the deficiency of the macromolecular co-reactant of $Ru(bpy)_3^{2+}$, which holds great promise for multisignal bioassay development. Moreover, the systematic clarification of the detailed mechanisms of converting the anodic or cathodic luminescence of $Ru(bpy)_3^{2+}$ by controlling the diameter of AuNPs in Au/rGOs should inspire further development of other luminescence enhancers of $Ru(bpy)_3^{2+}$ with excellent catalytic activity, such as single-atom catalysts, and can possibly be extended to other ECL luminophores using ROS as the co-reactants. Furthermore, the comparison of various ratiometric immunosensors and the new design of a single-luminophore co-reactant-based double anti-sandwich ratiometric immunosensors should provide new meaning for the dual-potential signal output luminophores, such as $Ru(bpy)_3^{2+}$, and pave the way for the development of more advanced multiple-signal strategies.

Materials and Methods

Materials

$HAuCl_4$, silver nitrate ($AgNO_3$), chloroplatinic acid ($HPtCl_6$), palladium chloride ($PdCl_2$), and sodium citrate were obtained from Aladdin Reagent Company. $Ru(bpy)_3^{2+}$ was acquired from Suna Tech Inc. Natural graphite powder (325 mesh) was purchased from Nanjing XFNANO Materials Tech Co. Ltd. Sodium borohydride ($NaBH_4$), ethanethiol, ascorbic acid, and isopropanol were obtained from Sinopharm Chemical Reagent Co. Ltd. N-Hydroxy succinimide (NHS; Guaranteed Reagent (GR)) and 1-ethyl-3-(3-di-methylaminopropyl) carbodiimide hydrochloride (EDC; GR) were acquired from Shanghai Medpep Co. Ltd. (Shanghai, China). BSA (96% to 99%, GR) was purchased from Biss Inc. (Beijing, China). CEA and antibodies were supplied by Beyotime Biotechnology Co. Ltd.

Table. Immunoassay of CEA in clinical serum samples using our method[a] and the reference method[b].

Sample	Proposed method (ng/ml)	Reference method (ng/ml)	Relative error (%)
1	269.13	283.0	−4.90
2	90.52	97.9	−7.54
3	31.90	29.2	9.25
4	15.30	14.9	2.68
5	1.35	1.24	8.87
6	0.82	0.8	2.50

[a]Provided as the mean of 3 repeated tests. In our approach, the sera were diluted 10,000-fold with PBS (pH = 7.4). RE, relative error.

[b]The reference method was the commercialized ECLIA that uses the Elecsys CEA, conducted on an electrochemiluminescent analyzer in the hospital.

(Shanghai, China). Human serum sample were provided by ChongQing Medical University. PBS (0.1 M (pH 7.4)) containing KH_2PO_4 and Na_2HPO_4 in an appropriate ratio with KCl (0.1 M) was used for ECL detection. All other chemicals were of analytical grade and used as received without further purification. All the aqueous solutions were freshly prepared and diluted with ultrapure water (≥18 MΩ; Milli-Q, Millipore).

Experimental design

Preparation of GO

GO was synthesized by the oxidation of natural graphite powder employing Hummers' method, with a few modifications [41]. Briefly, graphite powder (3.0 g) was added to concentrated H_2SO_4 (70 ml) and was vigorously agitated in an ice bath. Then, 9.0 g of $KMnO_4$ was gently added to maintain the suspension temperature below 20 °C. The reaction system was successively transferred to a 40 °C oil bath and aggressively agitated for approximately 30 min. After that, 150 ml of water was added, and the solution was agitated for 15 min at 95 °C. A further 500 ml of water was added, followed by a steady addition of 15 ml of H_2O_2 (30%), which changed the color of the solution from dark brown to yellow. To remove metal ions, the mixture was filtered and washed with 250 ml of 1:10 HCl aqueous solution. The resultant solid was dried in air and diluted to 600 ml to create an aqueous graphite oxide aqueous dispersion. Finally, it was dialysis-purified for 1 week using a dialysis membrane (Beijing Chemical Reagent Co., China) with a molecular weight cutoff of 8,000 to 14,000 g·mol^{-1} to eliminate the residual metal species. The resulting graphite oxide aqueous dispersion was then diluted to 1.2 l, agitated overnight, and sonicated for 30 min to exfoliate it to GO. The GO dispersion was then centrifuged at 3,000 rpm for 40 min to remove the unexfoliated graphite.

Preparation of rGO

To reduce GO to rGO, 2 mg of GO was dissolved in 2 ml of ultrapure water, and the resulting 2 mg/ml of GO and 2 ml of hydrazine hydrate were placed separately in 2 clean small beakers, with a large beaker covering both. After 6 h of stirring, the color of the GO fabric had changed from light brown to black, indicating the formation of rGO.

Preparation of Ab_2 bioconjugates

Initially, the as-prepared Au/rGO-2 was sonicated for 45 min before use. After that, 120 μl of the 2 mg/ml of Au/rGO-2 was dispersed in newly prepared EDC (0.01 mol/l)/NHS (0.002 mol/l) solution. A total of 120 ml of 10 μg·ml^{-1} of Ab_2 solution was added to the above solution and incubated at 4 °C for 10 h under constant temperature shaking conditions. After centrifugation (5000 rpm, 15 min), 120 ml of 1% BSA solution was added to block the nonspecific sites and oscillated at 4 °C for 2 h. The mixture was then centrifugated at 4000 rpm for 10 min. Finally, the obtained Au/rGO-2-Ab_2 was redistributed into 120 ml of pH 7.4 PBS solution and stored at 4 °C until use.

Fabrication procedure for the ratiometric ECL biosensor

The fabrication process of the ratiometric ECL immunosensor was shown in Fig. 5B. Before modification, the bare GCE was cleaned by physical polishing and chemical/electrochemical washing and checked in the reversible electrode reaction of the $Fe(CN)_6^{3-}/Fe(CN)_6^{4-}$ pair. Then, 5 μl of 2 mg/ml of Au/rGO-3 was dropped onto the cleaned GCE and dried at room temperature. Subsequently, 5 μl of the EDC/NHS solution was used to activate the carboxyl group of Au/rGO-3 for 30 min at 37 °C. After washing with ultrapure water, 5 μl of 20 μg/ml of antibody (Ab_1) was incubated on the modified electrode for 1 h at 37 °C. After removing the excess reagent, 5 μl of 1.0 wt% of BSA was dipped onto the modified electrode to block the nonspecific adsorption sites. Subsequently, 5 μl of CEA with different concentrations (10^{-1}, 10^{-2}, 10^{-3}, 10^{-4}, 10^{-5}, 10^{-6}, and 10^{-7} ng/ml) was added on the decorated electrode and incubated for 1 h at 37 °C. After washing with ultrapure water, a 5-μl Ab_2 bioconjugate was incubated on the modified electrode for 1 h at 37 °C to construct the ratiometric ECL immunosensor.

Application of the ratiometric sensing platform for bioanalysis

CEA was detected on a double antibody sandwich-modified electrode in a solution of 100 mM pH 6.0 PBS containing 1 mM $Ru(bpy)_3^{2+}$ at room temperature using an ECL method with 600 V of bias and a potential scan spanning from +1.5 to −2 V.

Electrochemical measurement

Cyclic voltammetry (CV)

CV was performed using a computer-controlled potentiostat (CHI660D) in a standard 3-electrode cell using Ag/AgCl (KCl saturated) electrode, a platinum wire as the counter electrode, and a GCE as the working electrode. Five microliters of Au/rGOs suspension was dropped onto a GCE with a diameter of 3 mm. The 3 electrodes were put into 0.1 M KOH solution. A flow of O_2 or N_2 was maintained for 40 min to achieve O_2-saturated (maximum concentration of dissolved oxygen) or O_2-free (substantial dissolved oxygen removal). The working electrode was cycled at least 5 times in the potential range from −2.0 to 1.5 V at a scanning rate of 100 mV/s.

Rotating disk electrode (RDE) measurements

The working electrode was prepared with the same method as that for CV. Before the measurement, a 30-min O_2 flow was utilized to saturate the electrolyte in the cell with oxygen. The LSV experiments were conducted on RDE at varying speeds

ranging from 225 to 3,600 rpm in O_2-saturated 0.1 M KOH at room temperature. The K–L plots (scatterplot of J^{-1} versus $\omega^{-1/2}$) were drawn on the basis of the different rotational speeds (ω) and their corresponding current density (J) at the same voltage (Fig. 4D). Then, the scatterplots obtained at different voltages were linearly fitted; the slop of which is k (inset in Fig. 4D). The electron transfer number (n) can be calculated using the K–L equation:

$$\frac{1}{J} = \frac{1}{J_L} + \frac{1}{J_K} = \frac{1}{B\omega^{1/2}} + \frac{1}{J_K}$$

$$B = 0.62nFC_{O_2}D_2^{2/3}\nu^{-1/6}$$

where J_K and J_L are the kinetic and diffusion-limiting current densities, respectively; n is the number of electrons transferred in the reduction; and ω is the angular velocity. When the rotational speed (ω) unit is taking as revolutions per minute (r/min = rpm), $B = 0.2nFC_{O_2}D_2^{2/3}\nu^{-1/6}$. After substituting all constants (F is the Faraday constant (96,485 C mol^{-1}), $C_{O2}$is the concentration of O_2 in the solution (1.2×10^{-6} mol cm^{-3}), D_{O2} is the diffusion coefficient of O_2 in solution (1.9×10^{-5} cm^2 s^{-1}), and ν is the kinematic viscosity of KOH (0.01 cm^2 s^{-1})) [42], the result is $B = 0.035n$. Because the K–L equation can be transformed to $J^{-1} = k\omega^{-1/2} + J_K{}^{-1}(k = B^{-1})$, k is equivalent to the slope of the K–L plots' fitted straight line, which can be derived from the plot. Then, substituting $B = 0.035n$ into $k = B^{-1}$ yields the electron transfer number n.

Acknowledgments

We would like to thank N. Ming, H. Zhi, and L. Jianming of the Chongqing Key Laboratory for Advanced Materials and Technologies of Clean Energies of the School of Materials and Energy, Southwest University for providing the rotating disc electrode equipment and for helpful discussions on topics related to this work. **Funding:** This work was supported by grants from the Natural Science Foundation of Chongqing (cstc2020jcyj-msxmX0330, cstc2021jsyj-yzysbA0057, and cstc2019jcyj-zdxmX0028), the National Natural Science Foundation of China (31971242 and 12032007), the Project of Tutorial System of Medical Undergraduate in Lab Teaching & Management Center in Chongqing Medical University (LTMCMTS202005 and LTMCMTS202110) and the JinFeng Laboratory Foundation of Chongqing (jfkyjf202203001), the Scientific and Technological Research Program of Chongqing Municipal Education Commission (KJQN202200426), the Scientific Research, the CQMU Program for Youth Innovation in Future Medicine (W0015), and the Innovation Experimental Project of Chongqing Medical University (SRIEP202105). **Author contributions:** S.W. conceived and designed the study. S.Z., Z.K., and Z.D. performed the experiments and collected the data. X.W. and X.L. contributed to experiments. K.H. analyzed the data. J.H. provided serum samples. G.W., G.Z., and Y.Z. supervised the study. **Competing interests:** The authors declare that they have no conflicts of interest regarding the publication of this article.

Data Availability

Data supporting the findings of this study are available in the main text or the Supplementary Materials. Additional data related to this paper may be requested from the authors.

Supplementary Materials

Fig. S1. (A) TEM image, (B) HAADF image, and (C) SEM image of Au/rGO.
Fig. S2. DPV lines of rGO and Au/rGO on GCE in PBS.
Fig. S3. EDS mappings of Au/rGO.
Fig. S4. XRD patterns of rGO and Au/rGOs.
Fig. S5. Zeta potential of GO, rGO, and Au/rGO.
Fig. S6. XPS survey spectra of rGO (A), Au/rGO (B), C1s deconvolution spectrum N1s peak (C), and Au4f region of Au/rGO (D).
Fig. S7. Raman spectrum of rGO and Au/rGOs.
Fig. S8. RDE lines of Au/rGO-1, Au/rGO-2, and Au/rGO-3 in O_2-saturated 0.1 M KOH.
Fig. S9. (A) RDE lines in O_2-saturated 0.1 M KOH at 1,600 rpm and (B) ECL line in 0.1 M $Ru(bpy)_3^{2+}$ of Au/rGO, Ag/rGO, and Pt/rGO.
Fig. S10. ECL performance of Au/rGO-2 and Au/rGO-3 under O_2, air, and N_2 atmospheres.
Fig. S11. ECL responses of Au/rGO-2 and Au/rGO-3 in $Ru(bpy)_3^{2+}$ with ROS inhibitor BQ, SOD, and isopropanol.
Fig. S12. ECL curves of Au/rGO-3/GCE in $Ru(bpy)_3^{2+}$ before and after it was electrochemically reduced.
Fig. S13. Oxygen and carbon atoms ratio of (A) Au/rGO-2 and (B) Au/rGO-3 before and after the reaction with $Ru(bpy)_3^{2+}$.
Fig. S14. ECL performance of AuNPs with different diameters (A), GO and rGO (B), and Au/GO-1 and Au/GO-2 as well as Au/rGO-1 and Au/rGO-2 (C) in $Ru(bpy)_3^{2+}$.
Fig. S15. Ultraviolet-visible absorption spectra of Au/rGO with different GO reduction degrees (A). The logarithm of the anodic to cathodic ECL luminescence intensity of $Ru(bpy)_3^{2+}$ reacting with Au/rGO with different rGO reduction times (B).
Fig. S16. The effect of (A) pH, (B) $C_{[Au/rGO-2]}/C_{[Au/rGO-3]}$, and (C) $Ru(bpy)_3^{2+}$'s concentration on $lg(I_c/I_a)$ signal output of the immunosensor.
Fig. S17. The comparison of Au/rGO-2 with traditional $Ru(bpy)_3^{2+}$'s cathodic co-reactant GSH, $K_2S_2O_8$, and H_2O_2.
Scheme S1. The schematic illustration for cathodic and anodic ECL reaction pathways.
Table S1. Comparison of the different potential-resolved platforms for ratiometric ECL immunoassay.
Table S2. The XPS atomic of C1s, N1s, O1s, and Au4f on Au/rGO synthesized at different concentrations of $HAuCl_4$

References

1. Liu X, Zhao S, Tan L, Tan Y, Wang Y, Ye Z, Hou C, Xu Y, Liu S, Wang G. Frontier and hot topics in electrochemiluminescence sensing technology based on CiteSpace bibliometric analysis. *Biosens Bioelectron*. 2022;113932.
2. Zanut A, Fiorani A, Canola S, Saito T, Ziebart N, Rapino S, Rebeccani S, Barbon A, Irie T, Josel HP, et al. Insights into the mechanism of coreactant electrochemiluminescence facilitating enhanced bioanalytical performance. *Nat Commun*. 2020;11(1):2668.
3. Chen M, Ning Z, Chen K, Zhang Y, Shen Y. Recent advances of electrochemiluminescent system in bioassay. *J Anal Test*. 2020;4(2):57–75.
4. Liang T-T, Qin X, Xiang Y, Tang Y, Yang F. Advances in nucleic acids-scaffolded electrical sensing of extracellular vesicle biomarkers. *TrAC Trends Anal Chem*. 2022;148:116532.

5. Lv W, Ye H, Yuan Z, Liu X, Chen X, Yang W. Recent advances in electrochemiluminescence-based simultaneous detection of multiple targets. *TrAC Trends Anal Chem*. 2020;123:115767.
6. Zhao J, Du J, Luo J, Chen S, Yuan R. A novel potential-resolved electrochemiluminescence immunosensor for the simultaneous determination of brain natriuretic peptide and cardiac troponin I. *Sensors Actuators B Chem*. 2020;311:127934.
7. Guo W, Ding H, Gu C, Liu Y, Jiang X, Su B, Shao Y. Potential-resolved multicolor electrochemiluminescence for multiplex immunoassay in a single sample. *J Am Chem Soc*. 2018;140(46):15904–15915.
8. Zhao J, He Y, Tan K, Yang J, Chen S, Yuan R. Novel ratiometric electrochemiluminescence biosensor based on BP-CdTe QDs with dual emission for detecting microRNA-126. *Anal Chem*. 2021;93(36):12400–12408.
9. Wang S, Zhu S, Kang Z, Chen Y, Liu X, Deng Z, Hu K, Wang G, Zhang Y, Zang G. Recent advances and future prospects of the potential-resolved strategy in ratiometric, multiplex, and multicolor electrochemiluminescence analysis. *Theranostics*. 2022;12(15):6779–6808.
10. Cao S-P, Luo Q-X, Li Y-J, Liang R-P, Qiu J-D. Gold nanoparticles decorated carbon nitride nanosheets as a coreactant regulate the conversion of the dual-potential electrochemiluminescence of Ru (bpy) 3 2+ for Hg 2+ detection. *Chem Commun*. 2020;56(42):5625–5628.
11. Han Z, Shu J, Liang X, Cui H. Label-free ratiometric electrochemiluminescence aptasensor based on nanographene oxide wrapped titanium dioxide nanoparticles with potential-resolved electrochemiluminescence. *Anal Chem*. 2019;91(19):12260–12267.
12. Qin Y, Wang Z, Xu J, Han F, Zhao X, Han D, Liu Y, Kang Z, Niu L. Carbon nitride quantum dots enhancing the anodic electrochemiluminescence of ruthenium (II) tris (2, 2′-bipyridyl) via inhibiting the oxygen evolution reaction. *Anal Chem*. 2020;92(23):15352–15360.
13. Zhang G-R, Bo-Qing X. Nano-size effect of Au catalyst for electrochemical reduction of oxygen in alkaline electrolyte. *Chin J Catal*. 2013;34(5):942–948.
14. Sasaki K, Naohara H, Choi YM, Cai Y, Chen WF, Liu P, Adzic RR. Highly stable Pt monolayer on PdAu nanoparticle electrocatalysts for the oxygen reduction reaction. *Nat Commun*. 2012;3(1):1115.
15. Kamiuchi N, Sun K, Aso R, Tane M, Tamaoka T, Yoshida H, Takeda S. Self-activated surface dynamics in gold catalysts under reaction environments. *Nat Commun*. 2060;9(1):2060.
16. Jeyabharathi C, Senthil Kumar S, Kiruthika GVM, Phani KLN. Aqueous CTAB-assisted electrodeposition of gold atomic clusters and their oxygen reduction electrocatalytic activity in acid solutions. *Angew Chem*. 2010;122(16):2987–2990.
17. Lee Y, Loew A, Sun S. Surface-and structure-dependent catalytic activity of Au nanoparticles for oxygen reduction reaction. *Chem Mater*. 2010;22(3):755–761.
18. Li D, Wang C, Tripkovic D, Sun S, Markovic NM, Stamenkovic VR. Surfactant removal for colloidal nanoparticles from solution synthesis: The effect on catalytic performance. *ACS Catal*. 2012;2(7):1358–1362.
19. Fan Q, Yang H, Ge J, Zhang S, Liu Z, Lei B, Cheng T, Li Y, Yin Y, Gao C. Customizable ligand exchange for tailored surface property of noble metal nanocrystals. *Research*. 2020;2020:2131806.
20. Liu R, Ye X, Cui T. Recent progress of biomarker detection sensors. *Research*. 2020;2020:7949037.
21. Zhang W, Xie H, Ma Z, Zhao H, Ren L. Graphene oxide-induced substantial strengthening of high-entropy alloy revealed by micropillar compression and molecular dynamics simulation. *Research*. 2022;2022:9839403.
22. Fan Y, Xiang Y, Shen H-S. Temperature-dependent mechanical properties of graphene/Cu nanocomposites with in-plane negative Poisson's ratios. *Research*. 2020;2020:5618021.
23. van Bokhoven JA, Miller JT. d Electron density and reactivity of the d band as a function of particle size in supported gold catalysts. *J Phys Chem C*. 2007;111(26):9245–9249.
24. Kolzunova L, Shchitovskaya E, Karpenko M. Polymethylolacrylamide/AuNPs nanocomposites: Electrochemical synthesis and functional characteristics. *Polymers*. 2021;13(14):2382.
25. Yin H, Tang H, Wang D, Gao Y, Tang Z. Facile synthesis of surfactant-free Au cluster/graphene hybrids for high-performance oxygen reduction reaction. *ACS Nano*. 2012;6(9):8288–8297.
26. Pal R, Wang L-M, Pei Y, Wang L-S, Zeng XC. Unraveling the mechanisms of O2 activation by size-selected gold clusters: Transition from superoxo to peroxo chemisorption. *J Am Chem Soc*. 2012;134(22):9438–9445.
27. Gewirth AA, Thorum MS. Electroreduction of dioxygen for fuel-cell applications: Materials and challenges. *Inorg Chem*. 2010;49(8):3557–3566.
28. Yuan Y, Han S, Hu L, Parveen S, Xu G. Coreactants of tris (2, 2′-bipyridyl) ruthenium (II) electrogenerated chemiluminescence. *Electrochim Acta*. 2012;82:484–492.
29. Kumar B, Kawawaki T, Shimizu N, Imai Y, Suzuki D, Hossain S, Nair LV, Negishi Y. Gold nanoclusters as electrocatalysts: Size, ligands, heteroatom doping, and charge dependences. *Nanoscale*. 2020;12(18):9969–9979.
30. Bard AJ, Faulkner LR. *Electrochemical methods: Fundamentals and applications*. New York (NY): Wiley; 2001.
31. Sachdeva H. Recent advances in the catalytic applications of GO/rGO for green organic synthesis. *Green Process Synth*. 2020;9(1):515–537.
32. Dong Y-P, Zhou Y, Wang J, Zhu J-J. Electrogenerated chemiluminescence resonance energy transfer between Ru (bpy) 32+ electrogenerated chemiluminescence and gold nanoparticles/graphene oxide nanocomposites with graphene oxide as coreactant and its sensing application. *Anal Chem*. 2016;88(10):5469–5475.
33. Jeyabharathi C, Senthil Kumar S, Kiruthika GVM, Phani KLN. Aqueous CTAB-Assisted electrodeposition of gold atomic clusters and their oxygen reduction electrocatalytic activity in acid solutions. *Angew Chem Int Ed*. 2010;49(16):2925–2928.
34. Lim D-H, Wilcox J. Mechanisms of the oxygen reduction reaction on defective graphene-supported Pt nanoparticles from first-principles. *J Phys Chem C*. 2012;116(5):3653–3660.
35. Miao W, Choi J-P, Bard AJ. Electrogenerated chemiluminescence 69: The Tris (2, 2′-bipyridine) ruthenium (II), (Ru(bpy)32+)/ Tri-*n*-propylamine (TPrA) system revisited A new route involving $TPrA^{\bullet+}$ cation radicals. *J Am Chem Soc*. 2002;124(48):14478–14485.
36. Zheng H, Zu Y. Highly efficient quenching of coreactant electrogenerated chemiluminescence by phenolic compounds. *J Phys Chem B*. 2005;109(33):16047–16051.
37. Wu X, Huang F, Duan J, Chen G. Electrochemiluminescent behavior of melatonin and its important derivatives in the presence of Ru(bpy)32+. *Talanta*. 2005;65(5):1279–1285.

38. Qi B-P, Zhang X, Shang B-B, Xiang D, Qu W, Zhang S. A facile method to sensitively monitor chlorinated phenols based on Ru (bpy) 32+ electrochemiluminescent system using graphene quantum dots as coreactants. *Carbon*. 2017;121:72–78.
39. Shao K, Wang B, Ye S, Zuo Y, Wu L, Li Q, Lu Z, Tan XC, Han H. Signal-amplified near-infrared ratiometric electrochemiluminescence aptasensor based on multiple quenching and enhancement effect of graphene/gold nanorods/G-quadruplex. *Anal Chem*. 2016;88(16):8179–8187.
40. Wang Y, Zhao G, Chi H, Yang S, Niu Q, Wu D, Cao W, Li T, Ma H, Wei Q. Self-luminescent lanthanide metal–organic frameworks as signal probes in electrochemiluminescence immunoassay. *J Am Chem Soc*. 2020;143(1):504–512.
41. Hummers WS Jr, Offeman RE. Preparation of graphitic oxide. *J Am Chem Soc*. 1958;80(6):1339–1339.
42. Yin P, Yao T, Wu Y, Zheng L, Lin Y, Liu W, Ju H, Zhu J, Hong X, Deng Z, et al. Single cobalt atoms with precise N-coordination as superior oxygen reduction reaction catalysts. *Angew Chem*. 2016;128(36):10958–10963.